# Upper crustal structure of Newberry Volcano from P-wave tomography and finite difference waveform modeling

Matthew W. Beachly,[1] Emilie E. E. Hooft,[1] Douglas R. Toomey,[1] and Gregory P. Waite[2]

[1] Seismic tomography combined with waveform modeling constrains the dimensions and melt content of a magma body in the upper crust at Newberry Volcano. We obtain a $P$-wave tomographic image by combining travel-time data collected in 2008 on a line of densely spaced seismometers with active-source data collected in the 1980s. The tomographic analysis resolves a high-velocity intrusive ring complex surrounding a low-velocity caldera-fill zone at depths above 3 km and a broader high-velocity intrusive complex surrounding a central low-velocity anomaly at greater depths (3–6 km). This second, upper-crustal low-velocity anomaly is poorly resolved and resolution tests indicate that an unrealistically large, low-velocity body representing $\sim$60 km$^3$ of melt could be consistent with the available travel times. The 2008 data exhibit low amplitude first arrivals and an anomalous secondary P wave phase originating beneath the caldera. Two-dimensional finite difference waveform modeling through the tomographic velocity model does not reproduce these observations. To reproduce these phases, we predict waveforms for models that include synthetic low-velocity bodies and test possible magma chamber geometries and properties. Three classes of models produce a transmitted $P$-phase consistent with the travel time and amplitude of the observed secondary phase and also match the observed lower amplitude first arrivals. These models represent a graded mush region, a crystal-suspension region, and a melt sill above a thin mush region. The three possible magma chamber models comprise a much narrower range of melt volumes (1.6–8.0 km$^3$) than could be constrained by travel-time tomography alone.

## 1. Introduction

[2] Geophysical imaging of crustal magma bodies improves our understanding of magma storage and ascent in the crust. The concept of a magma plumbing system has evolved over the past six decades from a diapir of melt or large spherical chamber to more geometrically complex systems ranging from multilevel networks of conduits and reservoirs [e.g., *Bons and Dougherty-Page*, 2001] to stratified mush zones overlain by melt lenses [e.g., *Sinton and Detrick*, 1992]. Imaging the geometry of magma feeder systems provides a critical constraint for understanding the geochemical evolution of magma, eruptive mechanisms, and caldera formation. In addition, estimating the volume of a magma body and its partial melt content can contribute to hazard assessment.

[3] An often-used geophysical technique for imaging magma bodies is seismic tomography, which constrains regions of low velocity and high attenuation [*Lees*, 2007]. However, due to wavefront healing, low-velocity bodies may not be resolved by the arrival time of the first seismic phase, especially if the bodies are smaller or deeper than the dominant seismic wavelength [*Nolet and Dahlen*, 2000]. Alternatively, interaction of seismic energy with a low-velocity anomaly often produces distinct secondary phases. Magma bodies have been successfully identified from secondary phases such as $P$-wave reflections [e.g., *Brown et al.*, 1980], $S$-wave reflections [*Sanford et al.*, 1973], converted $P$-to-$S$-wave transmissions [*Ferrucci et al.*, 1992] and reflections [*Durant and Toomey*, 2009], and even converted $S$-to-$P$-wave transmissions [*Sanford et al.*, 1973] and reflections [*Stroujkova and Malin*, 2000]. Because of the relatively sharp velocity and impedance contrast between magma bodies and the surrounding rock, secondary phases produced at these boundaries are often better suited for imaging magma bodies than travel-time tomography methods, which are sensitive to a path integral of the velocity structure.

[1] Department of Geological Sciences, University of Oregon, Eugene, Oregon, USA.
[2] Department of Geological and Mining Engineering and Sciences, Michigan Technological University, Houghton, Michigan, USA.

Corresponding author: E. E. E. Hooft, Department of Geological Sciences, University of Oregon, Eugene, OR 97403, USA. (emilie@uoregon.edu)
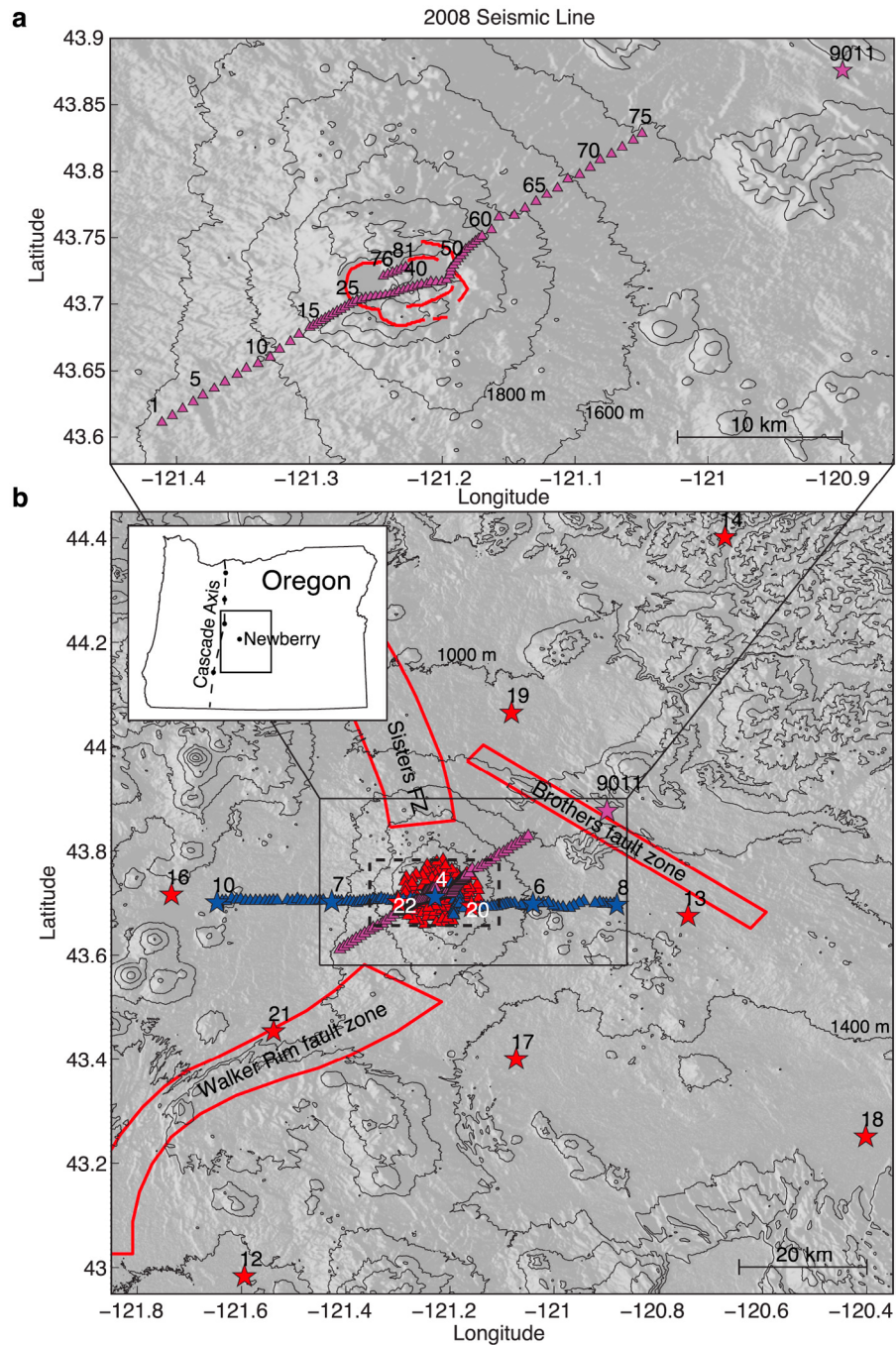
**Figure 1.** (a) Map of the 2008 seismic experiment on shaded topography with 200 m contour interval. The seismic line was 40 km long and centered on Newberry caldera. Stations (pink triangles) were spaced every 300 m near the volcano's center and 800 m on its flanks. Stations are labeled from 1 to 75 along the main line, and 76 to 81 along the inter-lake line. Note that the kink in the main line is due to the presence of the intracaldera lakes. Shot 9011 (star) of the High Lava Plains Experiment was 30 km northeast of the caldera. The shot occurred ~5 km south of the planned location. Exposed caldera ring fractures are marked in red [from *MacLeod et al.*, 1995]. (b) Map of the three seismic data sets used in the tomography inversion for upper crustal *P*-wave velocity structure. The USGS data collected in 1983 and 1984 are shown with blue and red symbols, respectively. The explosive sources are shown as numbered stars, the stations as triangles. Regions outlined in red show the location of the Walker-Rim, Sisters' and Brother's fault zones (taken from *Fitterman* [1988]). The dashed box shows the region covered by Figure 4. The box in the inset map of Oregon shows the location of Figure 1b east of the Cascade Arc.
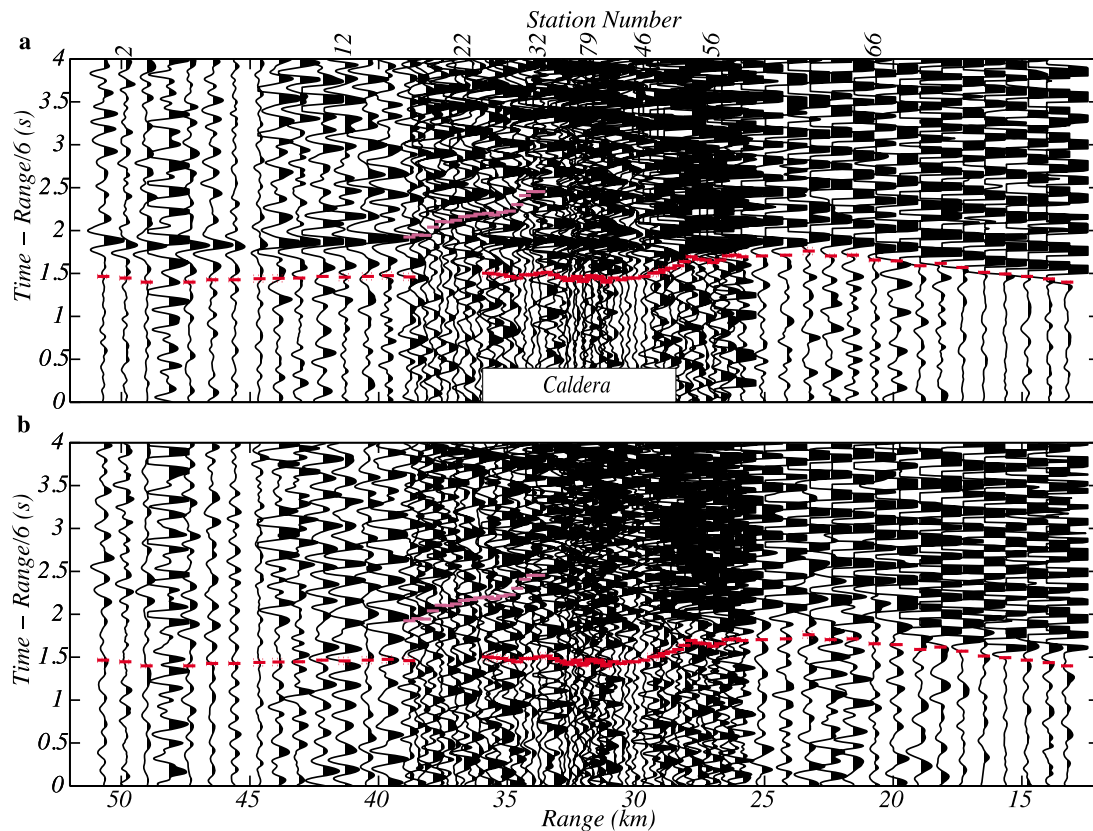
**Figure 2.** Seismic record sections from the 2008 experiment plotted as reduced travel time (6 km/s) versus reversed range. A 1–8 Hz Butterworth filter was applied to reduce noise. Amplitude scaling was fixed and trace amplitudes clipped at 0.8 km. (a) Vertical-component record section showing first-arrival *P*-wave picks (red) and secondary-phase picks (magenta). (b) Radial-component record section showing first-arrival *P*-wave picks (red) and secondary-phase *P* picks (magenta) from the vertical-component record section for comparison.

[4] Secondary phases have been used to successfully identify magma bodies in seismic experiments with densely sampled data sets such as those employing air gun sources [e.g., *Durant and Toomey*, 2009] and vibrators [*Brown et al.*, 1980]. Recognizing a secondary phase in the coda of the first arrival requires a dense sampling of the wavefield so that the phase can be identified across multiple seismograms and thus be attributed to a single common phenomenon. In 2008 we designed a seismic experiment that deployed a line of densely, evenly spaced seismometers on Newberry volcano in central Oregon and recorded a nearby explosive source. The experimental geometry resulted in a seismic record section with good trace-to-trace coherence that allowed us to identify low *P*-wave amplitudes and an anomalous secondary phase, which appear to originate beneath the volcano's caldera.

[5] In this study we use travel-time tomography combined with forward modeling of seismic amplitudes and arrival times of primary and secondary arrivals to better constrain the crustal seismic structure beneath Newberry Volcano. The seismic results are in turn used to infer the dimensions and melt content of the magma system beneath the volcano. We first use travel-time tomography to obtain a *P*-wave velocity model of the upper crustal structure at Newberry. This starting velocity structure initializes finite difference waveform models

designed to analyze the nature of the anomalous secondary phase. Waveform modeling of the tomographically recovered velocity structure does not generate the observed secondary phase nor match the amplitude variations of the first-arriving phase. In addition, resolution tests show that a low-velocity magma body is not well resolved by tomography. We run forward models for a range of synthetic low-Q, low-velocity bodies to test for the existence of magma chambers with various geometries and melt contents. To evaluate the models, we compare time, range, and amplitude of the secondary phase and amplitude of the first arrivals. Our results show that while a low-velocity body may be poorly resolved by tomography alone, a combination of tomography and finite difference modeling constrains the geometry and velocity of the anomalous region and thus places tighter constraints on the dimensions and melt content of the upper-crustal magma body.

## 2. Background

### 2.1. Geologic Background

[6] Newberry Volcano is a shield-shaped composite volcano located in central Oregon, 60 km east of the axis of the Cascade arc (Figure 1). Despite its low profile Newberry is volumetrically the largest volcano in the Cascade arc, with an estimated volume of 500 km$^3$ of lavas covering an area of
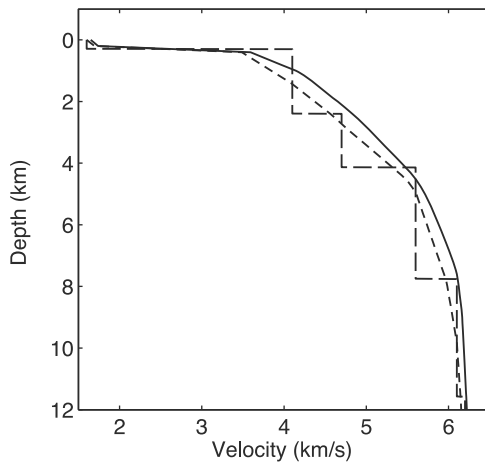
**Figure 3.** The 1D initial velocity models used in the tomographic inversion. The initial smooth gradient model (short dashed line) was estimated from the *Catchings and Mooney* [1988] refraction profile (long dashed line). Successive 3D inversions were averaged to obtain a better 1D starting model (solid line).

3000 km$^2$ [*Jensen et al.*, 2009]. Newberry's volcanism is thought to result from a combination of subduction zone magmatism, extensional tectonics and crustal weakness at the intersection of the Walker Rim, Sisters, and Brothers fault zones [*Fitterman*, 1988], and a northwestward propagating volcanic front that ends at Newberry. The volcanic front originated in southeastern Oregon ∼16 Ma and left a trail of rhyolites across the High Lava Plains [*Jordan et al.*, 2004]. This volcanic province may be related to the Columbia River flood basalts and the Yellowstone plume ∼17 Ma [e.g., *Humphreys et al.*, 2000; *Draper*, 1991]. Volcanism at Newberry began 0.5 Ma and multiple ash flow tuffs suggest that at least three caldera collapse events produced the central caldera, with the most recent event 80 ka [*Jensen et al.*, 2009].

[7] In addition to caldera collapses, evidence for a shallow magma storage system beneath Newberry includes a bimodal distribution of silicic and mafic eruptions. Silicic eruptions mainly occur within the caldera, such as the Big Obsidian Flow (1300 years old), and mafic eruptions occur outside the caldera, such as the Northwest Rift Zone eruptions of 7,000 years ago [*Mckay et al.*, 2009]. To cause this pattern, rising mafic magmas are thought to encounter a central, silicic magma storage system beneath the caldera [*MacLeod and Sherrod*, 1988]. The fresh mafic magma intrudes and underplates the silicic magma, causing it to erupt in the caldera, but elsewhere the unobstructed mafic magma erupts at the surface. It is likely that magma still resides at shallow depth beneath the caldera since a drill hole in the center of the caldera recorded a temperature of 265° at 932 m depth [*Keith and Bargar*, 1988], the highest drill hole temperature at this depth in the Cascades.

## 2.2. Geophysical Studies

[8] Previous geophysical studies at Newberry Volcano do not agree on the presence of a shallow crustal magma body. Electromagnetic studies did not detect the expected conductivity anomaly associated with a magma body, possibly because a shallower conductive layer obscured it [*Fitterman et al.*, 1988]. A teleseismic tomography study concluded that a magma chamber wider than its horizontal resolution limit of 5 km did not exist [*Stauber et al.*, 1988]. An active source tomography study with higher resolution resolved a low-velocity body at 3–5 km depth beneath the caldera and interpreted it as a magma chamber a few to several tens-of-km$^3$ in volume [*Achauer et al.*, 1988]. However, a later $P$-wave attenuation study of the same seismic data did not find a high-attenuation anomaly coincident with the low-velocity body and offered an alternative interpretation of the low-velocity anomaly as a hot, recently solidified pluton [*Zucca and Evans*, 1992]. *Zucca and Evans* [1992] suggest that with high temperature and gas-filled cracks a pluton could have low $P$-wave velocity and moderate $P$-wave attenuation. Other geophysical structures described in previous studies include a low-velocity caldera-fill zone surrounded by a high-velocity, high-gravity ring beneath the caldera ring faults that are attributed to an intrusive ring complex [*Achauer et al.*, 1988; *Gettings and Griscom*, 1988].

## 3. Seismic Data

### 3.1. 2008 Seismic Experiment

[9] The objective of our 2008 seismic experiment was to use a dense array of receivers in order to obtain good trace-to-trace coherence that would allow us to observe any secondary phase from anomalous structures beneath Newberry Volcano. We deployed 75 Mark Products L-22D short-period (2 Hz), three-component seismometers on a 40-km-long line centered on Newberry caldera (Figure 1a) in order to record a one ton, 85′ deep, explosive source from the contemporaneous High Lava Plains experiment [e.g., *Cox et al.*, 2010]. The seismometers were buried in a half meter of volcanic ash, oriented by compass, and calibrated for amplitude using a PASSCAL CalBox and BirdDog II. The seismometer spacing was 300 m in the caldera and on the upper flanks and 800 m on the outer flanks. An additional short, parallel line of six seismometers was located between the two lakes within the caldera, just north of the main line. The dense, even spacing of seismometers and near straight-line deployment ensured that the record section had enough trace-to-trace coherence to identify a secondary phase (Figure 2).

### 3.2. 2008 Seismic Record Section

[10] The 2008 seismic experiment successfully recorded first arrivals and a secondary phase on the vertical-component record section (Figure 2a). The first arrival shows a 0.5 s travel-time advance where it approaches the caldera (28 to 30 km range), coinciding with an amplitude reduction by a factor of 3. At the far side of the caldera (36 to 39 km range) the first-arrival amplitudes are so low that the first arrivals are difficult to observe. Coinciding with these ranges a secondary phase appears, with a prominent peak starting 0.8 s after the first arrival at 34 km range that appears to merge with a phase parallel to the first arrival at 39 km range. This parallel phase is present ∼0.5 s behind the first arrival throughout the seismogram and we attribute it to
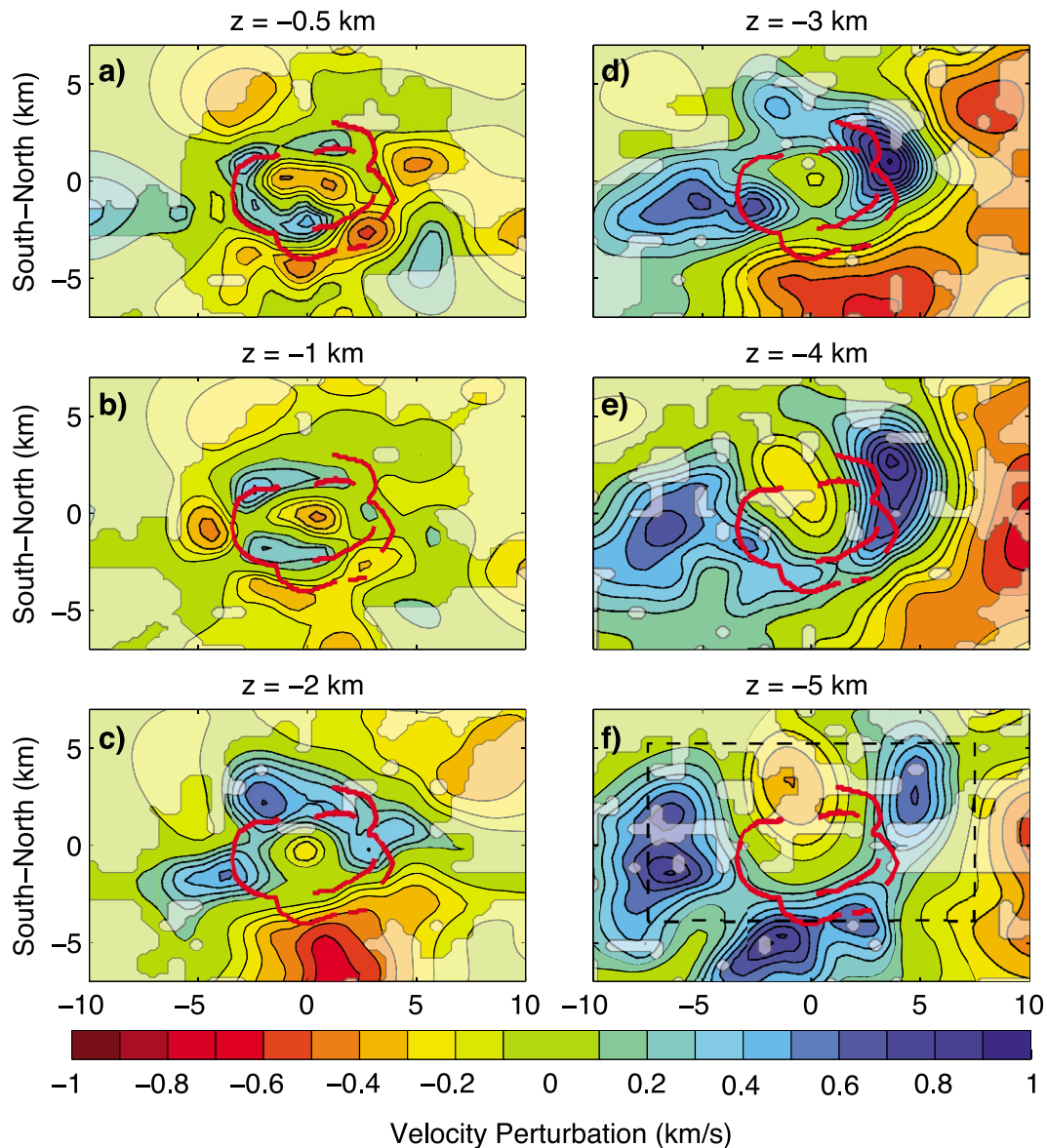
**Figure 4.** (a–f) Depth sections through the final *P*-wave velocity model of the tomography inversion. Velocity is colored as perturbation from the initial 1D velocity model with 0.1 km/s contours. A transparent overlay masks the velocity model where the DWS is less than one indicating where the velocity model is resolved, see text. Red lines show caldera ring faults mapped at the surface [*MacLeod et al.*, 1995]. Major features include a high-velocity ring that follows the caldera ring faults and surrounds a central low-velocity region above 2 km depth (Figures 4a and 4b), a much broader and higher magnitude high-velocity anomaly below 2 km depth (Figures 4c–4f), and a central low-velocity body below 3 km depth (Figures 4e and 4f). In Figure 4f, the region covered by Figure 7 is shown by the dashed box.

the source function of the explosion. A similar secondary phase is observed in the record section of shot 7 of the 1983 refraction experiment for waves traveling through Newberry from a different direction and at shorter ranges (Figure S1 in the auxiliary material).[1] The radial-component data (oriented toward the shot) generally has a lower signal-to-noise ratio suggesting poor horizontal coupling of the seismometers

(Figure 2b). The *P*-wave arrival and the secondary phase are more difficult to distinguish on the radial-component and no *S*-waves are evident.

## 4. *P*-Wave Tomography

[11] We invert travel times to obtain a *P*-wave velocity model of Newberry Volcano that images the upper crustal structure of the volcano and also serves as a starting model for finite difference forward modeling of the seismic wavefield. Our inversion differs from previous work
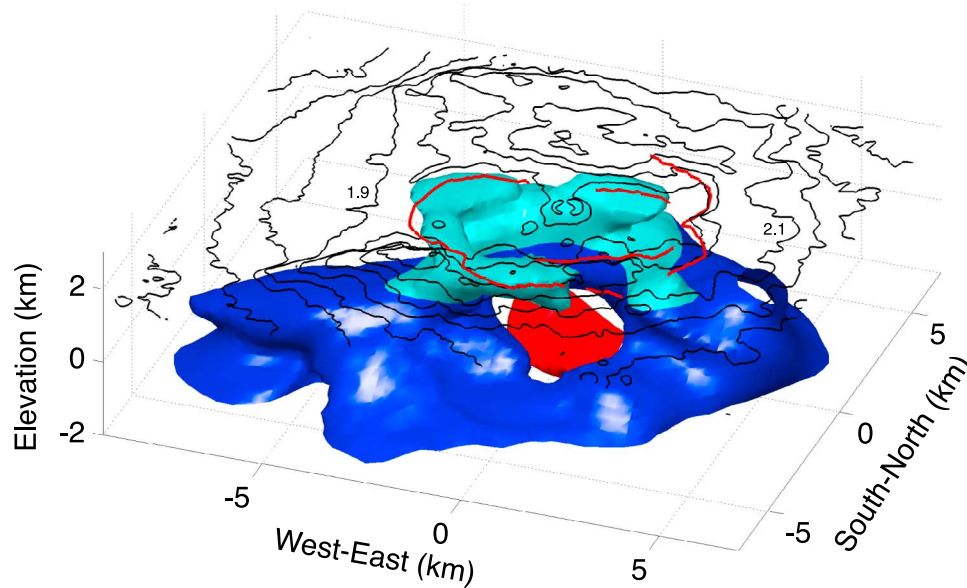
**Figure 5.** 3D representation of tomographically recovered velocity anomalies illuminated from the southeast. The view is from 20° east of south and 30° above horizontal. High-velocity structure is colored light blue above 1.5 km depth and dark blue below 1.5 km depth, contoured at +0.2 km/s velocity perturbation. The color difference distinguishes a possible structural difference between the shallow high-velocity ring and a broader, deeper high-velocity region. The central low-velocity body is colored red and contoured at −0.1 km/s velocity perturbation from 3 to 5 km depth. The shallow low-velocity anomaly within the caldera is not shown. At the surface, red lines show inferred ring fractures and black lines show 0.1 km topography contours.

at Newberry in three ways: we use a larger travel-time data set than in earlier work, a more densely parameterized inversion model that is damped with horizontal and vertical smoothing constraints [*Toomey et al.*, 1994], and a ray tracing method that uses graph theory [*Moser*, 1991] and incorporates topography.

### 4.1. P-Wave First Arrival Travel Times

[12] For the tomographic study we combine first-arrival, travel-time picks from the 2008 seismic experiment with data from two previous USGS experiments in 1983 and 1984. The 1983 seismic refraction line consisted of 120 seismometers deployed in a 60 km east-west line across Newberry Volcano and five shots spaced every 15 km along this line (Figure 1b) [*Cotton and Catchings*, 1989]. Seismometers and shots east of the tomography inversion region are not used. The 1984 experiment comprised an array of 122 seismometers distributed around the caldera and 12 shots (10 of which were useable) arranged around the caldera in three rings ranging ~7, 40, and 87 km from the center of the caldera [*Dawson and Stauber*, 1986]. We re-pick the 1983 and 1984 data sets, obtaining a total of 1007 P-wave first arrival travel times, with an average error of 18 msec for the 1980s data and 24 msec for the 2008 data (we tolerate higher error to include more data from the 2008 experiment).

### 4.2. Tomographic Inversion Method

[13] For forward modeling of travel times and raypaths, we parameterize the P-wave velocity model using nodes spaced 200 m and 100 m in the horizontal and vertical directions, respectively. The starting model for the tomographic analysis is a smooth one-dimensional model adapted from the seismic refraction profile of *Catchings and Mooney* [1988] that results in even ray coverage by depth. A smooth 1D model that better fits the data is obtained by inverting the travel-time data through the initial 1D model and averaging the result (Figure 3).

[14] We solve the inverse problem on a perturbational model with nodes spaced 400 m in the x and y directions and 200 m in the z direction. We conducted several tens of inversions to explore the effects of spatial smoothing and model damping on the resulting image (see *Toomey et al.* [1994] for details). For the results presented here, we used minimal model damping (1) and horizontal and vertical smoothing values (100 and 200, respectively) that resulted in a good fit to data and realistic model roughness. In addition, we inverted for static corrections to nine of the more distant events to remove the effect of unconstrained near-source structure.

[15] The sampling of tomographic velocity models may be approximated by the derivative weight sum (DWS), which is a weighted sum of the length of raypaths that influence a model parameter [*Toomey et al.*, 1990]. We calculated the
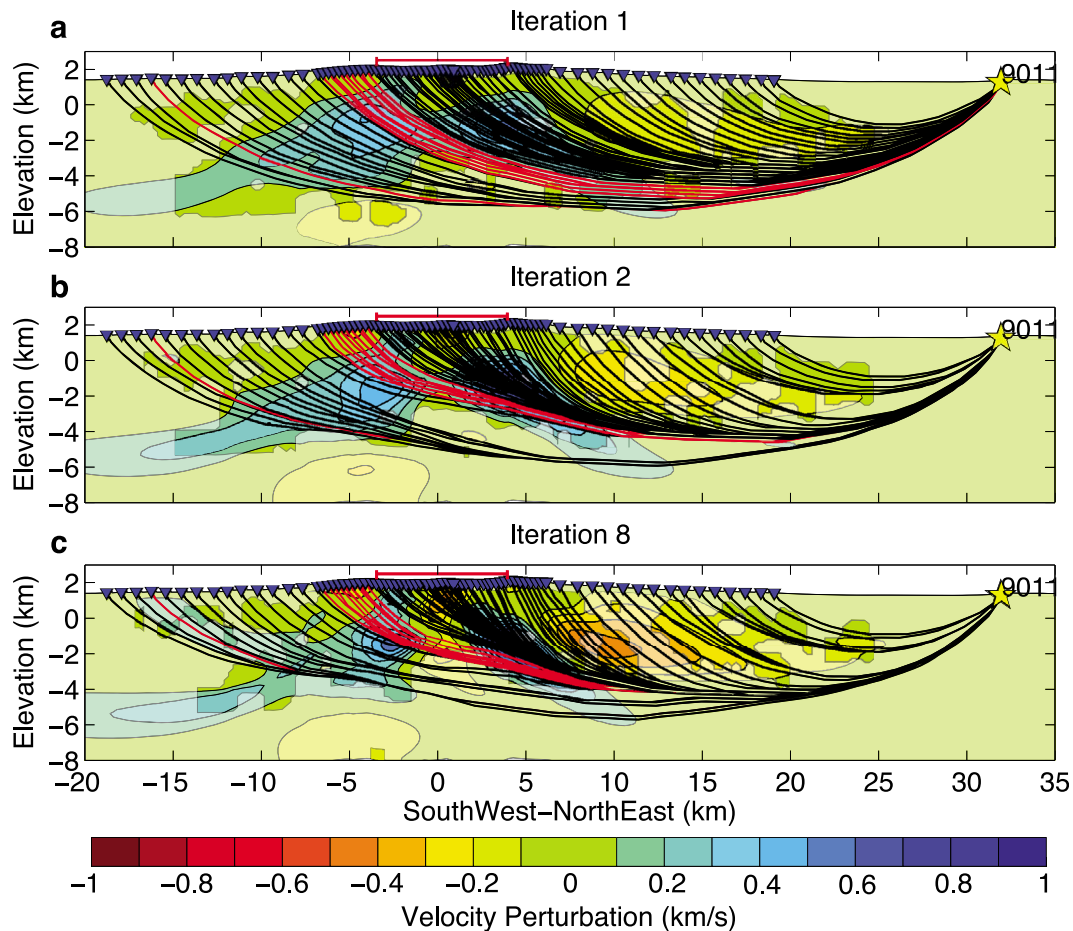
**Figure 6.** Development of ray bending around a low-velocity region at 3–6 km depth beneath the caldera during the tomographic inversion. Each panel shows the velocity perturbation and raypaths as they evolve for successive iterations. Raypaths (black and red lines), stations (triangles) and the shot (star) are shown along the 2008 seismic experiment; the profile is ∼1 km south of the center of the imaged low-velocity anomaly in the 3D tomography model. (a) The first iteration of the inversion solves for velocity perturbations along raypaths through the 1D starting velocity model. (b) The second iteration recalculates raypaths, which now bend above and below a region of average velocity between −2 and 2 km horizontal distance and −3 to −4 km elevation. (c) The eighth and final iteration shows ray bending that has fully developed around a region between −3 to 3 km horizontal range and −2 to −4 km elevation (∼4–6 km depth). A transparent overlay masks the velocity model where the DWS is less than one. Rays that appear to pass through the central masked region actually refract around the nearside. Red raypaths did not have travel-time picks due to low signal-to-noise ratio (Figure 2), probably resulting from spreading of energy where rays bend around the low-velocity region. A red bar shows the location of the caldera.

DWS on a 1 km grid, a spacing that is comparable to the seismic wavelength. In presenting our tomography results we use the DWS for the first iteration and a cut-off value of 1 to represent the sampling of the tomographic volume before rays are deflected by any high and/or low velocity regions that might develop during the inversion.

### 4.3. Tomography Results

[16] The tomographic result images the velocity structure beneath Newberry Volcano to a depth of 6 km (Figures 4 and 5). At shallow depths a ring-shaped, high-velocity anomaly underlies some of the inferred caldera ring faults. The high-velocity ring extends 7 km by 5 km east-west and north-south, respectively, and has a lateral thickness of 1–2 km. The high-velocity ring surrounds a central low-

velocity anomaly at 0.5 km depth that extends 4 km east-west and 2 km north-south. This low-velocity anomaly is 0.4 km/s lower than the average velocities at 0.5 km depth, and 0.8 km/s lower than the surrounding high-velocity ring. The low-velocity anomaly disappears around 2 km depth, where the high-velocity ring widens and increases in magnitude. The deeper, high-velocity region is more pronounced east and west of the caldera. At 3 km depth, the eastern high-velocity anomaly is 1 km/s faster than average and the western high-velocity anomaly is 0.6 km/s faster. Below 3 km depth the high-velocity zone expands and may be concentrated along regions of greater ray coverage and thus not reflect actual velocity structure. Outside the caldera, a broad low-velocity region extends to the south and east below 2.5 km depth. The full extent of this low-velocity
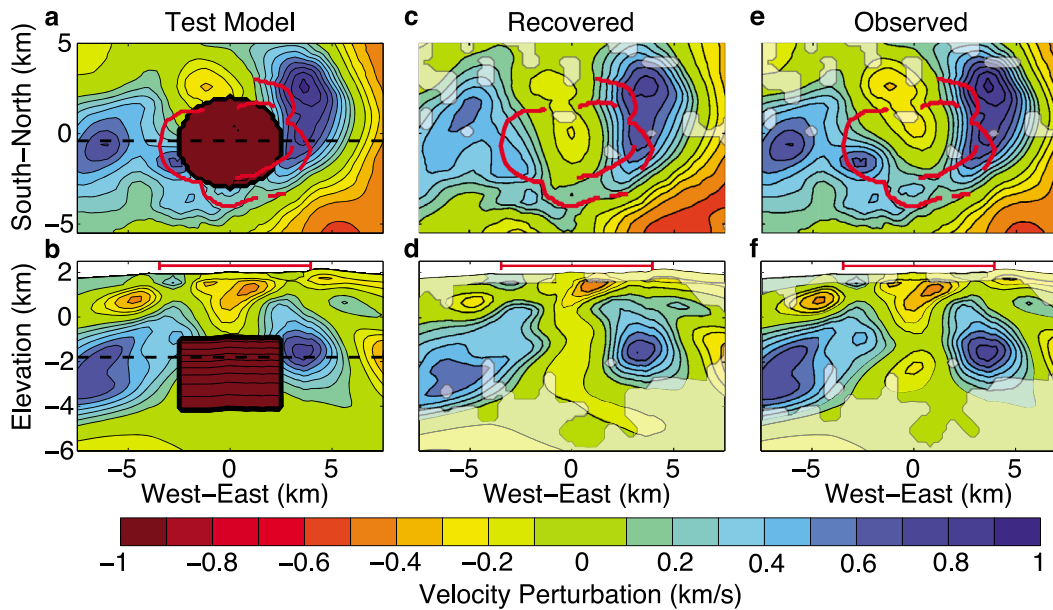
**Figure 7.** Tomographic resolution test of a large low-velocity body showing (a, c, e) map views and (b, d, f) depth sections. Dashed lines show where the profiles intersect. The red bar shows the location of the caldera. In Figures 7a and 7b, the synthetic model has a region 5 km wide between −1 and −4 km elevation with a velocity of 2.3 km/s (−2.7 to −3.5 km/s anomaly). Note that the magnitude of the low-velocity is below the −1 km/s limit of the color scale to keep the scale consistent with previous figures. In Figures 7c and 7d, a −0.2 km/s velocity anomaly is recovered from inversion of travel times for the synthetic model and the experimental geometry; this is less than 8% recovery. In Figures 7e and 7f, the tomography inversion of the actual observed travel-time data recovers a −0.2 km/s velocity anomaly with similar structure in map view and depth section.

region is poorly resolved, however it coincides with a gravity low [*Gettings and Griscom*, 1988]. A central low-velocity anomaly reappears beneath and to the north of the caldera at 4 km depth. The DWS reveals that coverage of the region below 5 km is poor and the actual extent and magnitude of the central low-velocity body is not well resolved.

[17] We investigate the resolution of the central low-velocity anomaly (at 3–6 km depth) by plotting ray sampling of this region and by performing several tomographic resolution tests. For the one-dimensional starting velocity model the ray coverage is good beneath the caldera (Figure 6a). As the tomographic iterations proceed, however, the presence of anomalously low velocities results in ray bending around the anomaly (Figures 6b and 6c). These results indicate that the poor resolution of the low-velocity body is caused primarily by its own presence, thus demonstrating the difficulty of resolving low-velocity bodies with travel-time tomography.

[18] Resolution tests further show that a low-velocity body with a much larger volume and magnitude than that which we recovered could be consistent with the observed travel-time data. We calculate synthetic travel-time data through a *P*-wave velocity model consisting of the tomographic velocity model on which is superimposed a cylindrical low-velocity anomaly with a volume of 59 km$^3$ and a velocity of 2.3 km/s, corresponding to pure melt (Figure 7). Tomographic inversion of the synthetic travel-time data recovers only a −0.2 km/s anomaly compared to the original −2.7 to −3.5 km/s anomaly. Note that the recovered synthetic low-velocity region is similar in horizontal extent and magnitude to that obtained from the actual data (although it is smeared

in vertical extent). This resolution test indicates that a ∼60 km$^3$ low-velocity body could be consistent with the available travel-time data.

[19] Comparison of the velocity model presented here with that obtained in earlier tomographic inversions shows similarities and differences that are due to our use of a greater quantity of data and a more finely parameterized, perturbational slowness grid. The earlier tomographic inversion of Newberry data incorporated only those 1984 shots that were outside of the array and had a 2-km perturbational grid spacing [*Achauer et al.*, 1988]. Our velocity models are similar in detecting a high-velocity ring at shallow depths and a deeper, broader high-velocity region to the west (velocity perturbation of up to 0.6 km/s at 4 km depth). The velocity models differ in that the current inversion also detects a broad high-velocity region to the east of the caldera – likely a result of including more data especially from the 2008 profile, which crosses this region and shows early arrivals. The velocity models both detect low velocities to the south and southeast of the caldera at <3 km depth. Finally, the velocity models are also similar in detecting the central low-velocity region, both in the uppermost crust (<2 km) and between 3 and 5 km depth (the velocity perturbation are of similar magnitude: 0.3 km/s at 4 km depth).

## 5. Waveform Forward Models

### 5.1. Finite Difference Waveform Modeling Methods

[20] The three-dimensional tomographic result is used as a starting model for waveform calculations using E3D, a
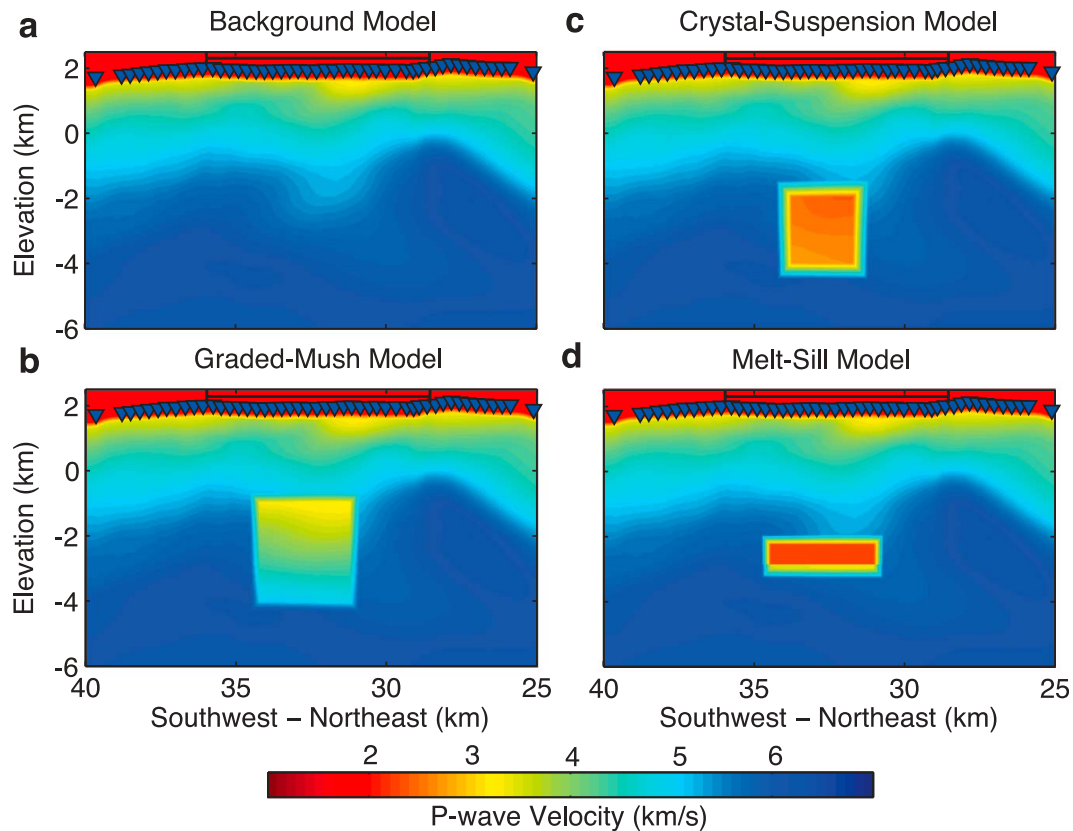
**Figure 8.** *P*-wave velocity parameterization for the finite difference waveform calculations. (a) The background model taken along the 2008 seismic profile through the 3D tomographic velocity model, and the preferred models for three classes of low velocity regions that represent different magmatic systems: (b) a graded-mush zone, (c) a crystal-suspension zone, and (d) a melt sill above a very thin mush zone. The dimensions and parameters used are given in Table 3. The black bar shows the location of the caldera.

2D/3D finite difference wave propagation code [*Larsen and Harris*, 1993]. We define a finite difference model for Newberry Volcano on a 2D grid extending 66 km in length (southwest to northeast) and 15 km in depth that includes the volcano's topography (from 2.5 km elevation to 12.5 km below sea level). The grid is evenly spaced in the x and z directions with 20 m nodal spacing, chosen to be roughly 1/10th of the shortest wavelength in the slowest part of the model (a 5 Hz *S*-wave traveling at 1 km/s near the surface has a wavelength of 200 m). We define the source signal by stacking the ten traces closest to the shot in a 0.44-s-long window starting at the first arrival. Finally, we choose a time step increment of 0.001 s, less than that required by the Courant Condition [*Courant et al.*, 1967], and a total run time of 15 s.

[21] The finite difference method requires that the *P*-wave velocity (*Vp*), *S*-wave velocity (*Vs*), density, *P*-wave quality factor (*Qp*), and *S*-wave quality factor (*Qs*) be defined (Figure 8). The 2D *P*-wave velocity model is obtained by interpolating velocities from the 3D tomographic model onto a profile trending southwest to northeast along the 2008 experiment. We calculate an *S*-wave velocity model and density model from the *P*-wave velocity model (Table 1). As for the *Qp* model, few useful relations exist between *Qp* and *Vp* in the literature, so we implement constant *Qp* layers that

are defined by *P*-wave velocity intervals (Table 1). Finally, we calculate the *Qs* model from the *Qp*, *Vp*, and *Vs* models (Table 1). The *Qs* and *Qp* models are assigned a central frequency of 5 Hz and higher and lower frequencies are attenuated to greater extents [*Larsen and Harris*, 1993]. In addition to representing attenuation structure within the primary modeling domain the *Qp* and *Qs* models also include high attenuation (*Qp* = 5) buffers on the left, bottom, and right edges of the model to absorb edge reflections, with cosine tapered inner regions to prevent *P*-to-*S*-wave conversions.

[22] To match the observed anomalous first-arrival amplitudes and the secondary phase we add a variety of structural anomalies to the background models that represent magma chambers with different geometries, velocity reductions, and attenuation values (Figure 8). The magma chambers are approximated as 2D blocks centered beneath Newberry caldera. We test magma chamber dimensions that range from −1 to −5 km in elevation (∼3 to 8 km depth) and 1 to 5 km in width. Within the anomalous block, we reduce *Vp*, *Vs*, density, *Qp*, and *Qs* properties to represent various partial melt contents. For models with partial melt we start with a *Vp* reduction such as 15% or 40%, and estimate the corresponding partial-melt content from *Chu et al.* [2010] and *Watanabe* [1993]. Note that *Watanabe*'s [1993]

**Table 1.** Physical Properties for the Background Finite Difference Waveform Model

| Model Parameter | Determination Method | Reference |
|---|---|---|
| P wave velocity ($Vp$) | Obtained from tomography | |
| S-wave velocity ($Vs$) | $Vs$(km/sec) $= 0.7858 - 1.2344\ Vp + 0.7949$ $Vp^2 - 0.1238\ Vp^3 + 0.0064\ Vp^4$ | Brocher's regression fit, *Brocher* [2005] |
| Density ($\rho$) | $\rho$(g/cm3) $= 1.6612\ Vp - 0.4721$ $Vp^2 + 0.0671\ Vp^3 - 0.0043\ Vp^4 + 0.000106\ Vp^5$ | Nafe-Drake curve from *Brocher* [2005] |
| P wave quality factor ($Qp$, constant layers) | $Qp = 50$ where $Vp < 3$ km/s $Qp = 100$ where $3$ km/s $\leq Vp < 4$ km/s $Qp = 150$ where $4$ km/s $\leq Vp < 5.6$ km/s $Qp = 200$ where $Vp > 5.6$ km/s | modified from *Brocher* [2005] |
| S-wave quality factor ($Qs$) | $Qs = 4/3(Vs/Vp)^2 Qp$ | theoretical relationship, *Clouser and Langston* [1991] |

work is based on experimental measurements of a Newberry rhyolite obsidian sample [*Murase and McBirney*, 1973]. From the partial-melt content we estimate a corresponding $Vs$ reduction and density (Table 2). Models with pure melt directly incorporate velocity and density values for melt from the literature. Unfortunately it is difficult to find appropriate $Q$ values for melt and partial melt in the literature, consequently we use a variety of methods to determine $Qp$ and $Qs$ (Table 2) and use $Qp = 8$ for partial melt and $Qp = 20$ for pure melt [*Collier et al.*, 2006; *Mavko*, 1980].

[23] To evaluate the results of the finite difference models, we generate synthetic seismic record sections and compare these to the observations. The finite difference calculation simulates the explosive source at the shot location along the 2D profile and generates seismic waveform traces at stations located along the profile. By generating waveform movies we can observe how the seismic waves interact with the structural anomaly and identify the origin of the anomalous secondary phase. We assess our synthetic magma-body models by comparing the amplitude of the synthetic first arrivals and the travel time, range, and amplitude of the synthetic secondary phase with the observations.

### 5.2. Waveform Modeling Results

[24] The results of the finite difference waveform modeling show that while the tomographically derived velocity model matches the observed first-arrival travel times, it does not produce a secondary phase nor the observed changes in first-arrival amplitudes. Figure 8a shows the background 2D velocity model taken along a profile through the 3D tomography model and Figure 9b shows the associated synthetic seismogram. Note that the synthetics do not reveal a secondary phase and over-predict the amplitude of the primary phase. To produce the observed secondary phase, a low-velocity body is required. A similar transmitted *P*-wave was attributed to a shallow magma chamber at Krafla Volcano, Iceland, and first-arrival amplitude reductions have also been observed and attributed to shallow magma chambers [*Brandsdóttir et al.*, 1997; *Gudmundsson et al.*, 1994]. In the example in Figure 10, snapshots of propagating wavefronts show that a transmitted *P*-wave phase becomes delayed and focused upward within the low-velocity body. The synthetics show that the first arrival is a lower-amplitude *P*-wave that traveled above the low-velocity region. Note that the waveform modeling predicts no reflected phase from the top of the low-velocity body due to the upward incidence of the wavefront, and only predicts weak *P*-to-*S*-wave conversions. The weak *P*-to-*S* conversions may be a result of the limit of finite difference calculations to describe *S*-waves where there are such low velocities and wavelengths are less than the grid spacing. However, we also note that there is no evidence for *P*-to-*S* conversions in the actual data.

**Table 2.** Magma Body Physical Property Parameterization[a]

| Magma-Body Parameter | Determination Method | Reference |
|---|---|---|
| $Vp$ (melt) | $Vp = 2.3$ km/s | *Murase and McBirney* [1973] |
| $Vp$ (partial melt) | %$Vp$ reductions are chosen a priori | |
| $Vs$ (melt) | $Vs = 0$ km/s | |
| $Vs$ (partial melt) | %$Vs$ reduction values are estimated from charts for corresponding $Vp$ values | *Chu et al.* [2010], *Watanabe* [1993] and *Sato et al.* [1989] |
| $\rho$ (melt) | $\rho = 2$ g/cm$^3$ | *Murase and McBirney* [1973] |
| $\rho$ (partial melt) | $\rho_{\text{partial melt}} = \phi_{\text{melt}}\rho_{\text{melt}} + \phi_{\text{solid}}\rho_{\text{solid}}$, $\phi$ represents volume concentration | *Murase and McBirney* [1973] |
| $Qp$ (melt) | $Qp = 20$, an intermediate value for bubble-free melt on chart | *Collier et al.* [2006] |
| $Qp$ (partial melt) | $Qp = 8$, the chart does not consider partial melt contents above 3% | *Mavko* [1980] |
| $Qs$ (partial melt $> \sim 30\%$) | $Qs = 10,000$, to stabilize model[b] | |
| $Qs$ (partial melt $< \sim 30\%$) | $Qs = 4/3(Vs/Vp)^2 Qp$ | *Clouser and Langston* [1991] |

[a]Methods differ based on whether the magma body includes melt (100% melt) or partial melt (ranges of $\sim$10–30% partial melt).
[b]We use a very high $Qs$ value (10,000) in cases with low $Vs$ to keep the finite difference calculations stable. This has little effect on the results since $S$ waves do not travel through these regions.
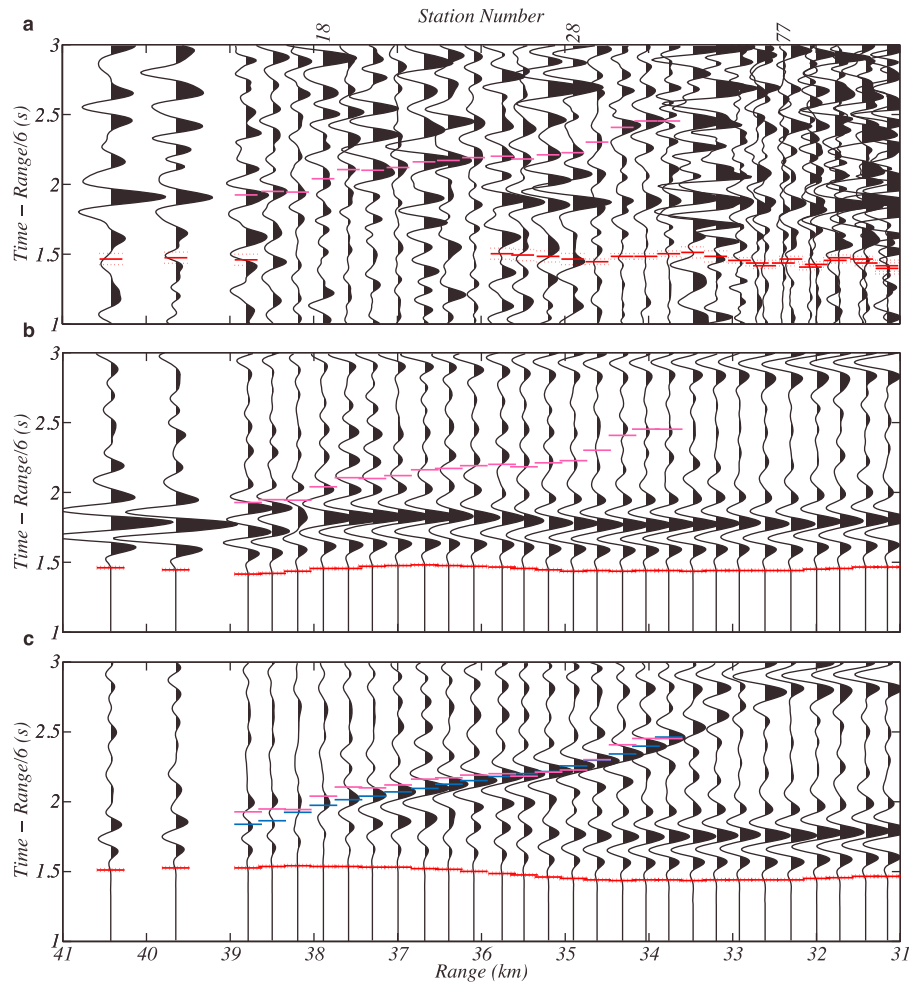
**Figure 9.** Observed and synthetic record sections for the 2008 experiment zoomed in on the secondary phase plotted with the same settings as in Figure 2. (a) Record section of the observed data showing the pick of the peak of the observed secondary phase (magenta) and the first-arrival time picks (red). (b) Synthetic seismic record section for the background model taken from the tomographic inversion. The background model does not produce a secondary-phase nor the reduction in first-arrival amplitude at ranges greater than 34 km. (c) Synthetic seismic record section for the mush-zone model (Figure 8b). The prominent peak of the secondary phase is shown (blue). In Figures 9b and 9c, the observed secondary-phase picks (magenta) and first-arrival picks (red) are shown for comparison.

[25] We obtain models that are better constrained than was possible with travel time tomography alone by using forward modeling to match the observed secondary-phase travel times and the amplitude variations of the primary and secondary phases. We superimpose low-velocity bodies on the background model to represent three types of magmatic systems: a graded-mush zone, a crystal suspension, and a melt sill above a thin mush zone (Figure 8) [*Caricchi and Burlini*, 2008]. We test different geometries for each model type to estimate the optimum depth and dimensions for each class of low-velocity body and find three preferred models from over 140 models tested. Figure 11 shows synthetic seismic record sections for the best models in each of the three classes. The results discussed below show that an anomalous volume with velocities lower than those recovered by travel-time tomography is required to produce a secondary phase and to reduce first-arrival amplitudes.

### 5.3. Description of Models

[26] The first class of model contains a low-velocity, high-attenuation body that represents a graded-mush zone. Of over fifty different geometries tested we find that a 3-by-3 km$^2$ anomaly from −1 to −4 km elevation (∼3–6 km depth) best matches the observations (Figure 11a). The low-velocity region has a linear gradient of *P*-wave velocity (*Vp*) reduction from 40% at the top to 15% at the bottom (Figure 8b and Table 3), representing a compacting mush zone with 26 ± 6% partial melt at the top and 11 ± 4% partial melt at the bottom (Table 2). A mush zone with this range of partial-melt could have tubes or films of melt between the boundaries of crystal grains, but not enough melt to completely separate the grains [e.g., *Caricchi and Burlini*, 2008].

[27] The second class of model represents a magma body with crystals suspended in partial melt. This class of
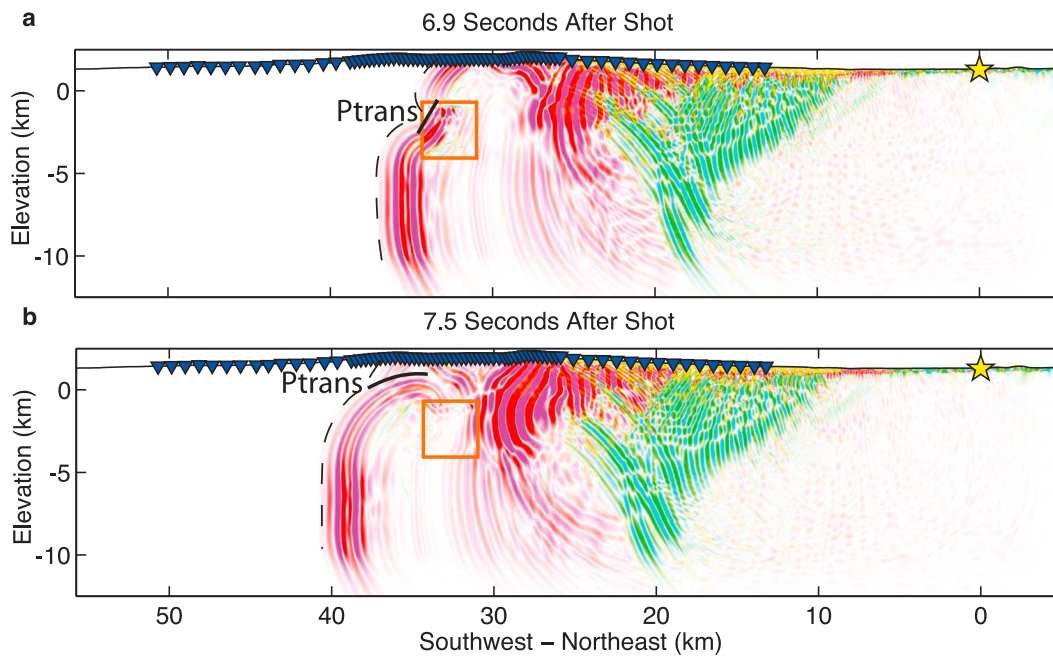
**Figure 10.** Snapshots of waveforms propagating through the mush-zone model (Figure 8b) during the finite difference calculations; *P*-waves are pink and *S*-waves are green. (a) At 6.9 s after the shot the first-arriving *P*-wave (dashed line) is delayed in the low-velocity body (orange box) and becomes a delayed and transmitted *P*-wave phase (*Ptrans*, solid line). (b) At 7.5 s after the shot this secondary phase (*Ptrans*) approaches the surface at 35 to 39 km range after the first-arriving wavefront (dashed) that traveled above the low-velocity body. Notice the wavefront healing and the reduced amplitude of the first-arriving wavefront (dashed).

model also produces a transmitted and delayed *P*-wave (Figure 11b) although the structural anomaly has smaller dimensions and a higher velocity reduction in comparison to the previous class of models. We find that a 2-by-2 km² low-velocity body from −2 to −4 km elevation (∼4 to 6 km depth) with a *Vp* reduction of 55% matches the data well (Figures 8c and 11b and Tables 2 and 3). This model could represent a magma body with 33 ± 8% partial melt. A magma body with this much partial melt would have isolated solid grains suspended within melt, possibly requiring convection to keep the grains from settling [*Marsh*, 1988]. Thus we use a constant *Vp* reduction throughout the low-velocity body and a *Vs* of 0 km/s because the lack of solid grain network would not support the transmission of *S* waves.

[28] The third and final class of model includes a thinner low-velocity body consistent with a melt sill above a thin mush zone that represents the settling of crystal grains as the melt cools. The geometry that best matches the seismic observations has a melt region 600 m thick and 4 km wide at −2.3 to −2.9 km elevation (∼4.3 to 4.9 km depth), overlying a mush region 100 m thick and 4 km wide at −2.9 to −3 km elevation (Figures 8d and 11c and Tables 2 and 3). In comparison with the previous two models the depth to the top of this anomaly is slightly deeper and it has the lowest *P*-wave velocities.

### 5.4. Analysis of Amplitude and Travel Time

[29] The travel time of the secondary phase is the sum of the time for the transmitted *P* wave to travel through the low-velocity body and reach the surface. A small low-velocity

body with a greater velocity reduction such as the suspended mush-zone model delays the secondary phase similarly to a larger low-velocity body with a lower velocity reduction such as the graded-mush-zone model. In addition, a secondary phase from a small, slightly deeper low-velocity body, such as the melt-sill model, reaches the surface at the same time as that from a volumetrically larger, shallower low-velocity body such as the graded-mush-zone model. Varying the exact lateral and vertical dimensions and velocity reduction of the low-velocity regions also affects the secondary phase by changing its time-distance slope and the ranges at which it is observed. The amplitude of the secondary phase is mainly controlled by the quality factor, *Q*, of the low-velocity body. The dimensions and the velocity reduction of the low-velocity body control the proportion of the wavefront that is trapped and converted into a transmitted *P*-wave and also affect the number of cycles that the transmitted wave travels through low *Q*.

[30] To evaluate the synthetic models we compare the amplitude and travel-time of the synthetic and observed secondary phases. We calculate the root-mean square (RMS) travel-time misfit for the prominent peak of the secondary phase (Figure 12a). Figure 12b shows the logarithm of the RMS amplitude of the secondary phase in a 0.5 s window centered on the travel-time pick plotted as a function of range. To adjust for site site-specific amplification, we normalize each seismogram by the RMS amplitude of the noise in a 1 s window before the first arrival. To compare synthetic and observed amplitudes, we normalize both seismograms by the average RMS amplitude of the ten arrivals
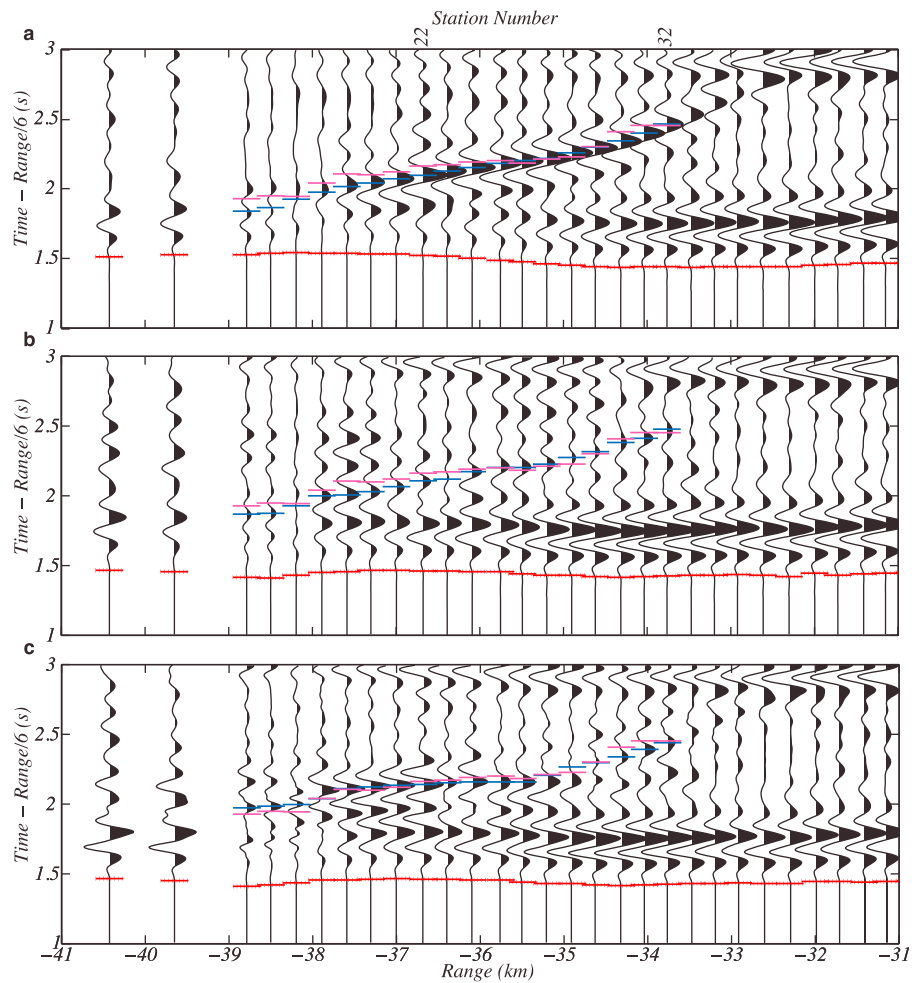
**Figure 11.** Comparison of synthetic record sections for the three preferred low-velocity models (Figure 8) zoomed in on the secondary phase. The record sections are plotted with the same settings as in Figure 2 and the prominent peak of the secondary phase (blue) and picks of the observed secondary-phase (magenta) and first-arrival (red) are shown. The models represent three magmatic systems: (a) a graded-mush zone (Figure 8b), (b) a crystal-suspension zone (Figure 8c), and (c) a melt sill above a very thin mush zone (Figure 8d).

just before the secondary phase appears (25.9–28.6 km range). Of the geometries and velocities tested for each class of model, the three preferred models best match the secondary-phase travel times and amplitudes. The RMS travel time misfits are similar (0.035 to 0.053 s) and the RMS amplitude misfits are also comparable (0.58 to 0.75). The melt-sill model has the best fit to both the travel time and

amplitude of the secondary phase while the graded and suspended mush models are similar.

[31] We also evaluate the synthetic models by fitting the amplitude of the first arrivals (Figure 13). In the finite difference calculations, the first-arrival amplitude of energy sampling the anomalous region is mainly controlled by the dimensions of the low-velocity body, since its size

**Table 3.** Dimensions and Physical Properties of the Three Preferred Models[a]

| Model | Partial Melt | $Vp$ | $Vs$ | $\rho$ | $Qp$ | $Qs$ |
|---|---|---|---|---|---|---|
| Mush zone | | | | | | |
| (top) elev. = −1 km | 26 ± 6% | −40%, 3.2 km/s | −75%, 0.9 km/s | 2.4 g/cm$^3$ | 8 | 3 |
| (bottom) elev. = −4 km | 11 ± 4% | −15%, 4.9 km/s | −20%, 2.6 km/s | 2.6 g/cm$^3$ | 8 | 0.9 |
| Crystal suspension | | | | | | |
| (top) elev. = −2 km | 33 ± 8% | −55%, 2.4 km/s | 0 km/s | 2.4 g/cm$^3$ | 8 | 10,000 |
| (bottom) elev. = −4 km | 33 ± 8% | −55%, 2.7 km/s | 0 km/s | 2.5 g/cm$^3$ | 8 | 10,000 |
| Melt sill | | | | | | |
| (melt) elev. = −2.3–2.9 km | 100% | 2.3 km/s | 0 km/s | 2.0 g/cm$^3$ | 20 | 10,000 |
| (mush) elev. = −2.9–3 km | 26 ± 6% | −40%, 3.4 km/s | −75%, | 2.5 g/cm$^3$ | 8 | 10,000 |

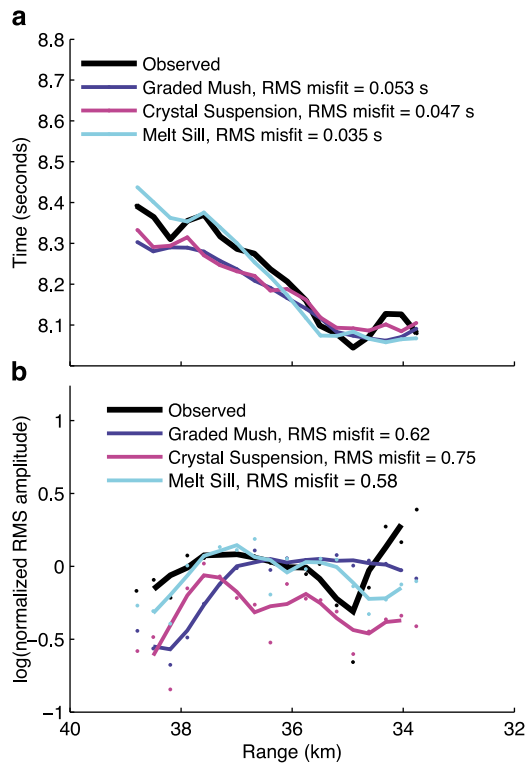[a]Properties are determined using the methods in Table 2.

**Figure 12.** (a) Plot of secondary phase travel-time (picked on the most prominent peak) versus range for the observed data (black) and the three preferred waveform models (colors). The RMS misfit for each model is calculated in linear space. (b) Plot of secondary phase RMS amplitude in a 0.5 s window centered on the travel-time picks. Secondary-phase RMS amplitudes are normalized by noise and by the average, first-arrival RMS amplitude of ten reference traces. The data points (dots) are smoothed with a three-point moving average (lines).

determines the region of the first-arrival wavefront that is obstructed. First-arrival amplitudes decrease due to spreading of energy around the obstructed region and subsequent wavefront healing. To evaluate the models, we calculate the RMS misfit of the amplitude of the observed and synthetic primary phases. The normalized RMS amplitude of a first arrival is calculated in a 0.3 s window starting at the first-arrival travel-time pick. We note that the RMS amplitude of the first arrivals decreases by a factor of 3 (Figure 2a). This abrupt and localized decrease is unlikely to be due to scattering in the shallow crust of the caldera [*Paulatto et al.*, 2010] since this effect would also influence the amplitude of the secondary arrival.

[32] When we compare the modeled and observed first arrival amplitudes, the background model has the highest RMS misfit (0.87) since it predicts first-arrival amplitudes up to 5 times higher (0.7 log units) than the observed amplitudes at ranges greater than 33 km (Figure 13). The presence of a low-velocity region in the synthetic models obstructs first-arrival energy, resulting in first-arrival amplitudes up to three times (0.5 log units) lower than those of the background model at ranges greater than 33 km (Figure 13). The RMS misfits of the first-arrival amplitudes are similar for the three preferred models (0.44 to 0.52), with

the melt-sill model and the graded-mush models having the lowest RMS misfit of 0.44. The misfit calculation may be biased because it weights observations from 30 to 36 km more heavily than those from 39 to 51 km since the stations are less densely spaced in the latter ranges. The range dependence of the RMS amplitudes (Figure 13) indicates that, at ranges of 34 to 38 km, the first-arrival amplitudes of the graded-mush model best match the observed data because there is a large amplitude reduction that is consistent with the signal-to-noise being too low to pick observed first arrivals at these ranges. However, at longer ranges, 39 to 51 km, the first-arrival amplitudes of the melt-sill model are in better agreement with the observed data. We consider the three models to fit all the available observations to a similar degree so that none of the classes of magmatic systems can be ruled out.

## 6. Discussion

[33] We first interpret the tomography results and then discuss how the finite difference waveform modeling allows us to better constrain the upper crustal magma system at Newberry Volcano. The tomography results reveal a heterogeneous velocity structure beneath the volcano. The velocity variation of these features may result from differences in porosity, lithology, temperature and/or partial melt. Our interpretation of these features considers the integrated history of Newberry Volcano, involving at least one caldera collapse along the inner ring faults, magma emplacement, north-south trending rift zones facilitating eruptions, and a central magma chamber beneath the caldera (Figure 14).

[34] At shallow depths (<2 km) we identify a high-velocity, ring-like anomaly within the caldera that encompasses an inner-caldera low-velocity zone. We interpret the low-velocity zone to be porous, caldera-fill deposits in the
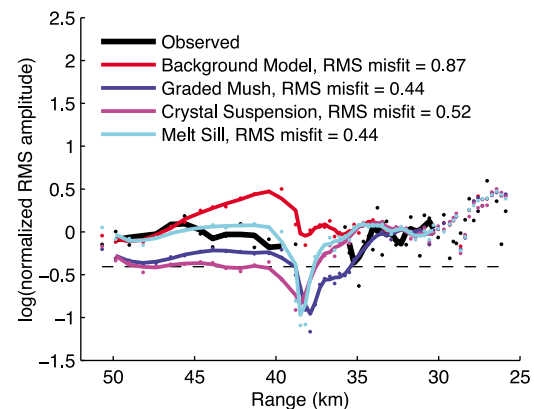


**Figure 13.** Comparison of synthetic and observed first-arrival amplitudes showing normalized first-arrival RMS amplitude versus range for the observed data (black) and the three preferred waveform models (colors). The normalized RMS is calculated in a 0.3 s window after the first arrival travel-time pick. Data at less than 25 km range are not used in the RMS misfit calculations to prevent higher amplitudes at closer ranges from swamping the effects of the low-velocity body. A dashed line indicates the normalized noise level, below which signal is difficult to observe. The data points (dots) are smoothed with a three-point moving-average (lines).
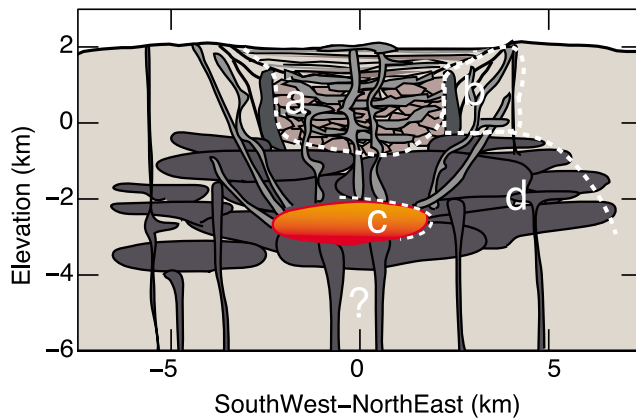
**Figure 14.** Geological interpretation of the subsurface structure of Newberry Volcano based on the tomographic and finite difference waveform modeling results. Region a is the caldera-fill zone consisting of layers of tephra, porous lavas, and rhyolite domes in the upper 1 km, and collapsed pre-caldera rocks in the lower 1 to 3 km. Silicic dikes and sills likely intrude this region. Region b is the intrusive-ring complex surrounding the caldera-fill zone. This region may consist of ring-dikes formed during caldera collapse, dikes intruded into ring faults during uplift and/or later dikes that feed eruptions on the caldera rim. Region c is the magma body. Here we show the molten sill case with a thin mush region at the bottom, consistent with the melt-sill waveform model (Figures 8d and 9c). Region d is the deeper intrusive complex composed of stalled dikes, sills, and remnant magma chamber plutons.

upper 500 m, possibly due to layers of tuff or rhyolitic domes [*Keith and Bargar*, 1988; *MacLeod and Sherrod*, 1988]. Below this depth (500 m to 2 km), low velocities are associated with porous, fractured lava flows that dominate the drill core below 500 m and which may be flows that post-date caldera collapse or the top of a central block that sank during caldera collapse. We interpret the surrounding high-velocity ring to be an intrusive ring complex because it underlies the faults encircling the caldera (Figure 4). Higher velocities may result from the intruded rock being more competent than its surroundings. The intrusive ring complex could be formed by either ring-dikes or cone-sheets. In the case of ring dikes, the subsided region consisted of a relatively intact block during "piston collapse" while magma extruded into fractures around this block, solidifying as ring-shaped dikes [e.g., *Cole et al.*, 2005; *Lipman*, 1997; *Marti et al.*, 1994]. Alternatively, cone-sheets may have been emplaced around the edge of the subsided zone [*Achauer et al.*, 1988] during pre-collapse uplift or during a later episode of resurgence. Dikes associated with eruptions along the caldera rim that post-date caldera collapse, such as the craters on the eastern caldera rim and the interlake obsidian flow [*MacLeod et al.*, 1995], may also contribute to the high-velocity ring.

[35] At greater depths (>2 km), we attribute high-velocities to an intrusive complex. The high-velocity region below 2 km depth is wider than the shallow high-velocity ring (15 km east-west by 8 km north-south at 2.5 km depth) and also greater in magnitude. We attribute these characteristics

to a larger volume of intrusive material built up by many intrusive events. The concentration of higher velocities east and west of the caldera may be related to the east-west extensional setting at Newberry Volcano. In this scenario rising mafic magma intrudes and solidifies around Newberry Volcano except where fractures along the Northwest Rift Zone, trending north-south through Newberry Volcano (Figure 1b), facilitate eruptions at the surface [*Mckay et al.*, 2009]. Intrusions east and west of the Northwest Rift Zone may not erupt as easily and consequently build up relatively larger intrusive complexes.

[36] The tomography results also reveal a central low-velocity body beneath 3 km depth. However, this low-velocity body is poorly resolved and may be consistent with structural features that range from the tomographically imaged anomaly to a much larger low-velocity volume (over 50 km$^3$). We consider the tomographically recovered anomaly to be the smallest low-velocity body required by the travel time data, and it may be attributed to a hot, fractured pluton [*Zucca and Evans*, 1992]. The tomographically imaged, low-velocity body has a P-wave velocity of 5.5 km/s at 5 km depth; to achieve this velocity by thermal effects requires a temperature of ~1800°C (for granite at 5 km depth d$Vp$/d$T$ = $-3.9 \times 10^{-4}$ km/s°C, $Vp$ = 6.2 km/s and $T$ = 85°C [*Christensen and Mooney*, 1995]). Since the solidus of granite is 700–900°C at this depth (100 MPa), depending on H$_2$O content [*Holtz et al.*, 2001], this temperature is not feasible. To achieve such low velocities a granitic pluton would have to be fractured. Velocity and porosity measurements on granite samples predict values ranging from 0.6% to 3% porosity [*Fourmaintraux*, 1975; *Christensen*, 1989]. Such porosities are plausible at 5 km depth and thus a fractured pluton could be consistent with the tomography results.

[37] At the other extreme our resolution tests indicate that a magma chamber ~60 km$^3$ in volume with a velocity of 2.3 km/s can also be consistent with the travel time data (Figure 7). This P-wave velocity cannot be explained with fluid-filled fractures and was chosen to correspond to pure melt. To more closely constrain the size and velocity reduction of the low-velocity body we supplement our tomography analysis with finite difference waveform modeling.

[38] In comparison with travel-time tomography, the finite difference modeling imposes stronger limits on the range of low-velocity bodies that are consistent with the observed secondary phase and first-arrival amplitudes. Indeed the tomographically recovered, low-velocity region does not satisfy these observations (Figures 9b, 12, and 13). We find that the graded mush-zone model is the feature with the smallest velocity reduction that is consistent with all the seismic observations. The mush zone represents a 3-by-3 km$^2$ region of interstitial melt between a matrix of compacting crystal grains; partial melt decreases from 26 ± 6% at the top to 11 ± 4% at the bottom. Assuming that this anomaly represents the cross section of a cylinder in 3D, it contains a total melt volume of 3.9 ± 0.8 km$^3$ ($V_{melt} = \phi_{avg}V_{cyl}$, where $\phi_{avg}$ is the average volume fraction of melt and $V_{cyl}$ is the volume of the cylinder). This percentage of melt may remain locked up in mush and may not erupt unless it is sufficiently reheated by intruding magma [*Bachmann and Bergantz*, 2006].

[39] We consider the crystal-suspension model to be the anomaly with a mid-range velocity reduction and the melt-sill model to be the feature with the lowest velocities that is

consistent with the observed secondary phase. The crystal-suspension model is 2-by-2 km$^2$, represents a region of 33 ± 8% partial-melt and contains a melt volume of 2.1 ± 0.5 km$^3$. The melt-sill model has a low-velocity anomaly representing pure melt ($\phi$ = 100%, 4 km wide and 600 m high) overlying a thin mush region ($\phi$ = 26%, 100 m high) and contains a melt volume of 7.9 ± 0.1 km$^3$. We find that the three preferred finite difference models predict a range of melt volumes between 1.6 and 8.0 km$^3$. This is a much narrower range of melt volume than can be constrained by the tomographic analysis, which permits melt volumes ranging from 0 to ~60 km$^3$.

[40] Geologic observations provide further insight into the nature of the magma system beneath Newberry Volcano. The Big Obsidian Flow that erupted 1300 years ago is rhyolitic and lacks phenocrysts, except for in mafic inclusions, implying that at that time the source was a silicic melt with no suspended crystals or mush [*Linneman and Myers*, 1990]. The mafic inclusions may have been incorporated from wall rock, fresh injection of mafic magma, or a separate mush region [*Linneman and Myers*, 1990]. We calculate that in 1300 years a ~420 m thick melt sill would solidify [*Turcotte and Schubert*, 2002]. Similarly any larger melt body would have significantly decreased in melt volume in 1300 years. We infer that our preferred magma chamber models are either the result of cooling of a larger magma body or that they were created by intrusions that postdate the eruption of the Big Obsidian Flow.

[41] The melt volumes predicted by our models are larger than the total eruptive volume associated with the Big Obsidian Flow, which ejected 0.16 km$^3$ of lava, tephra, and ash [*Sherrod and MacLeod*, 1979; *MacLeod and Sherrod*, 1988]. The lack of eruptions in the last 1300 years and the absence of earthquakes within 15 km of the caldera during the last two decades [*Moran*, 2004] suggest that any shallow magma body is quite stable. However, while no uplift has been detected during the last 15 years, uplift was measured between 1931 and 1994 and is possibly associated with a 0.06 km$^3$ intrusion at 10 km depth [*Dzurisin*, 1999]. In this case, the magma system may have been replenished at least once since the Big Obsidian Flow eruption 1300 years ago. If magma intrudes into the upper crust today, there may be associated seismicity, although volcano inflation also occurs aseismically [*Dzurisin et al.*, 2006]. InSAR data as well as the network of eight seismometers and GPS stations installed by the USGS in 2011 monitor Newberry Volcano for any volcanic unrest that would accompany future replenishment of the Newberry magma system.

## 7. Conclusions

[42] This study highlights the importance of using finite difference waveform modeling of secondary phases and of first arrival amplitudes in combination with seismic *P*-wave tomography to constrain the dimensions and properties of upper crustal magma bodies. We successfully recorded a secondary-phase at Newberry Volcano with a seismic experiment that used a densely spaced line of seismometers and an explosive source. We combine first-arrival travel-time data from our seismic experiment and two previous active-source experiments for a *P*-wave tomography inversion and image the velocity structure of Newberry Volcano to 6 km depth.

The tomography image reveals major structural features including a high-velocity intrusive ring complex, a low-velocity caldera-fill region, a deeper high-velocity intrusive complex, and a deeper, central low-velocity body that may be a magma body but is poorly resolved. Resolution tests show that the first-arrival travel-time data could be consistent with low-velocity features ranging from a hot-fractured pluton to a ~60 km$^3$ melt region.

[43] Finite difference waveform models closely reproduce the observed secondary phase with a transmitted *P*-wave that travels through a central low-velocity body. Using finite difference waveform forward modeling we find the optimum dimensions for low-velocity bodies representing three classes of magmatic systems: a graded-mush, a crystal-suspension, and a melt-sill over a thin mush zone. We optimized dimensions and depth of each type of body by comparing the secondary-phase in synthetic seismograms to the observed secondary phase in terms of travel-time and amplitude and also by comparing first-arrival amplitudes. The finite difference waveform calculations result in a narrower range of possible melt volumes than can be obtained with the tomographic analysis, 1.6 to 8 km$^3$, and constrain the magma body to lie between 3 and 6 km depth.

## References

Achauer, U., J. Evans, and D. Stauber (1988), High-resolution seismic tomography of compressional wave velocity structure at Newberry Volcano, Oregon Cascade Range, *J. Geophys. Res.*, *93*(B9), 10,135–10,147, doi:10.1029/JB093iB09p10135.

Bachmann, O., and G. Bergantz (2006), Gas percolation in upper-crustal silicic mushes as mechanism for upward heat advection and rejuvenation of near-solidus magma bodies, *J. Volcanol. Geotherm. Res.*, *149*, 85–102, doi:10.1016/j.jvolgeores.2005.06.002.

Bons, P., and J. Dougherty-Page (2001), Stepwise accumulation and ascent of magmas, *J. Metamorph. Geol.*, *19*, 627–633, doi:10.1046/j.0263-4929.2001.00334.x.

Brandsdóttir, B., W. Menke, P. Einarsson, R. S. White, and R. K. Staples (1997), Färoe-Iceland Ridge Experiment: 2. Crustal structure of the Krafla central volcano, *J. Geophys. Res.*, *102*(B4), 7867–7886, doi:10.1029/96JB03799.

Brocher, T. M. (2005), Empirical relations between elastic wavespeeds and density in the Earth's crust, *Bull. Seismol. Soc. Am.*, *95*(6), 2081–2092, doi:10.1785/0120050077.

Brown, L., C. Chapin, A. Sanford, and S. Kaufman (1980), Deep structure of the Rio Grande rift from seismic reflection profiling, *J. Geophys. Res.*, *85*(B9), 4773–4800, doi:10.1029/JB085iB09p04773.

Caricchi, L., and L. Burlini (2008), Propagation of P and S-waves in magmas with different crystal contents: Insights into the crystallinity of magmatic reservoirs, *J. Volcanol. Geotherm. Res.*, *178*, 740–750, doi:10.1016/j.jvolgeores.2008.09.006.

Catchings, R., and W. Mooney (1988), Crustal structure of east central Oregon: Relation between Newberry Volcano and regional crustal structure, *J. Geophys. Res.*, *93*(B9), 10,081–10,094, doi:10.1029/JB093iB09p10081.

Christensen, N. I. (1989), Reflectivity and seismic properties of the deep continental crust, *J. Geophys. Res.*, *94*(B12), 17,793–17,804, doi:10.1029/JB094iB12p17793.

Christensen, N., and W. Mooney (1995), Seismic velocity structure and composition of the continental crust: A global view, *J. Geophys. Res.*, *100*(B6), 9761–9788, doi:10.1029/95JB00259.

Chu, R., D. Helmberger, D. Sun, J. Jackson, and L. Zhu (2010), Mushy magma beneath Yellowstone, *Geophys. Res. Lett.*, *37*, L01306, doi:10.1029/2009GL041656.

Clouser, R. H., and C. A. Langston (1991), Qp-Qs relations in a sedimentary basin using converted phases, *Bull. Seismol. Soc. Am.*, *81*(3), 733–750.

Cole, J. W., D. M. Milner, and K. D. Spinks (2005), Calderas and caldera structures: A review, *Earth Sci. Rev.*, *69*, 1–26, doi:10.1016/j.earscirev.2004.06.004.

Collier, L., J. W. Neuberg, N. Lensky, V. Lyakhovsky, and O. Navon (2006), Attenuation in gas-charged magma, *J. Volcanol. Geotherm. Res.*, *153*, 21–36, doi:10.1016/j.jvolgeores.2005.08.009.

Cotton, J., and R. Catchings (1989), Data report for the 1983 US Geological Survey East-central Oregon Seismic Refraction Experiment, *U.S. Geol. Surv. Open File Rep.*, *89-124*, 60 pp.

Courant, R., K. Friedrichs, and H. Lewy (1967), On the partial difference equations of mathematical physics, *IBM J. Res. Dev.*, *11*, 215–234, doi:10.1147/rd.112.0215.

Cox, C. M., G. R. Keller, S. H. Harder, and S. Klemperer (2010), Raytrace models from the High Lava Plains (HLP) controlled-source experiment, *Seismol. Res. Lett.*, *81*(2), 332.

Dawson, P. B., and D. A. Stauber (1986), Data report for a three-dimensional high-resolution P-velocity structural investigation of Newberry Volcano, Oregon, using seismic tomography, *U.S. Geol. Surv. Open File Rep.*, *86-352*, 90 pp.

Draper, D. S. (1991), Late Cenozoic bimodal magmatism in the northern basin and range province of southeastern Oregon, *J. Volcanol. Geotherm. Res.*, *47*(3–4), 299–328, doi:10.1016/0377-0273(91)90006-L.

Durant, D., and D. Toomey (2009), Evidence and implications of crustal magmatism on the flanks of the East Pacific Rise, *Earth Planet. Sci. Lett.*, *287*(1–2), 130–136, doi:10.1016/j.epsl.2009.08.003.

Dzurisin, D. (1999), Results of repeated leveling surveys at Newberry Volcano, Oregon, and near Lassen Peak Volcano, California, *Bull. Volcanol.*, *61*(1–2), 83–91, doi:10.1007/s004450050264.

Dzurisin, D., M. Lisowski, and C. W. Wicks (2006), Geodetic observations and modeling of magmatic inflation at the Three Sisters volcanic center, central Oregon Cascade Range, USA, *J. Volcanol. Geotherm. Res.*, *150*, 35–54, doi:10.1016/j.jvolgeores.2005.07.011.

Ferrucci, F., A. Hirn, G. De Natale, J. Virieux, and L. Mirabile (1992), P-Sv conversions at a shallow boundary beneath Campi Flegrei caldera (Italy): Evidence for the magma chamber, *J. Geophys. Res.*, *97*(B11), 15,351–15,359, doi:10.1029/92JB00888.

Fitterman, D. (1988), Overview of the structure and geothermal potential of Newberry Volcano, Oregon, *J. Geophys. Res.*, *93*(B9), 10,059–10,066, doi:10.1029/JB093iB09p10059.

Fitterman, D., W. Stanley, and R. Bisdorf (1988), Electrical structure of Newberry volcano, Oregon, *J. Geophys. Res.*, *93*(B9), 10,119–10,134, doi:10.1029/JB093iB09p10119.

Fourmaintraux, D. (1975), Quantification of the discontinuities of rock and rock masses-methods and applications, *Bull. Liaison Lab Ponts Chaussees*, *75*, 69–76.

Gettings, M., and A. Griscom (1988), Gravity model studies of Newberry Volcano, Oregon, *J. Geophys. Res.*, *93*(B9), 10,109–10,118, doi:10.1029/JB093iB09p10109.

Gudmundsson, O., B. Brandsdóttir, W. Menke, and G. E. Sigvaldason (1994), The crustal magma chamber of the Katla Volcano in south Iceland revealed by 2-D seismic undershooting, *Geophys. J. Int.*, *119*, 277–296, doi:10.1111/j.1365-246X.1994.tb00928.x.

Holtz, F., W. Johannes, N. Tamic, and H. Behrens (2001), Maximum and minimum water contents of granitic melts generated in the crust: A reevaluation and implications, *Lithos*, *56*, 1–14, doi:10.1016/S0024-4937(00)00056-6.

Humphreys, E., K. Dueker, D. Schutt, and R. Smith (2000), Beneath Yellowstone: Evaluating plume and nonplume models using teleseismic images of the upper mantle, *GSA Today*, *10*(12), 1–7.

Jensen, R., J. Donnelly Nolan, and D. Mckay (2009), A field guide to Newberry Volcano, Oregon, in *Volcanoes to Vineyards: Geologic Field Trips Through the Dynamic Landscape of the Pacific Northwest, Field Guide*, vol. 15, pp. 53–79, Geol. Soc. of Am., Boulder, Colo., doi:10.1130/2009.fld015(03).

Jordan, B. T., A. L. Grunder, R. A. Duncan, and A. L. Deino (2004), Geochronology of age-progressive volcanism of the Oregon High Lava Plains: Implications for the plume interpretation of Yellowstone, *J. Geophys. Res.*, *109*, B10202, doi:10.1029/2003JB002776.

Keith, T., and K. Bargar (1988), Petrology and hydrothermal mineralogy of US Geological Survey Newberry 2 drill core from Newberry Caldera, Oregon, *J. Geophys. Res.*, *93*(B9), 10,174–10,190, doi:10.1029/JB093iB09p10174.

Larsen, S., and D. Harris (1993), Seismic wave propagation through a low-velocity nuclear rubble zone, Lawrence Livermore Natl. Lab., Livermore, Calif., doi:10.2172/10130414.

Lees, J. M. (2007), Seismic tomography of magmatic systems, *J. Volcanol. Geotherm. Res.*, *167*(1–4), 37–56, doi:10.1016/j.jvolgeores.2007.06.008.

Linneman, S., and J. Myers (1990), Magmatic inclusions in the Holocene rhyolites of Newberry volcano, central Oregon, *J. Geophys. Res.*, *95*(B11), 17,677–17,691, doi:10.1029/JB095iB11p17677.

Lipman, P. (1997), Subsidence of ash-flow calderas: Relation to caldera size and magma-chamber geometry, *Bull. Volcanol.*, *59*, 198–218, doi:10.1007/s004450050186.

MacLeod, N., and D. Sherrod (1988), Geologic evidence for a magma chamber beneath Newberry Volcano, Oregon, *J. Geophys. Res.*, *93*(B9), 10,067–10,079, doi:10.1029/JB093iB09p10067.

MacLeod, N., D. Sherrod, L. Chitwood, and R. Jensen (1995), Geologic map of Newberry volcano, Deschutes, Klamath, and Lake Counties, Oregon, *U.S. Geol. Surv. Misc. Invest. Ser., Map I-2455*, 2 sheets, scale 1:62,500.

Marsh, B. (1988), Crystal capture, sorting, and retention in convecting magma, *Geol. Soc. Am. Bull.*, *100*(11), 1720–1737, doi:10.1130/0016-7606(1988)100<1720:CCSARI>2.3.CO;2.

Marti, J., G. Ablay, and L. Redshaw (1994), Experimental studies of collapse calderas, *J. Geol. Soc.*, *151*, 919–929, doi:10.1144/gsjgs.151.6.0919.

Mavko, G. M. (1980), Velocity and attenuation in partially molten rocks, *J. Geophys. Res.*, *85*(B10), 5173–5189, doi:10.1029/JB085iB10p05173.

Mckay, D., J. Donnelly Nolan, R. Jensen, and D. Champion (2009), The post-Mazama northwest rift zone eruption at Newberry Volcano, Oregon, in *Volcanoes to Vineyards: Geologic Field Trips Through the Dynamic Landscape of the Pacific Northwest, Field Guide*, vol. 15, edited by J. E. O'Connor et al., pp. 91–110, Geol. Soc. of Am., Boulder, Colo., doi:10.1130/2009.fld015(05).

Moran, S. C. (2004), Seismic monitoring at Cascade volcanic centers, 2004: Status and recommendations, *U.S. Geol. Surv. Sci. Invest. Rep.*, *2004-5211*, 28 pp.

Moser, T. J. (1991), Shortest path calculation of seismic rays, *Geophysics*, *56*(1), 59–67.

Murase, T., and A. R. McBirney (1973), Properties of some common igneous rocks and their melts at high temperatures, *Geol. Soc. Am. Bull.*, *84*(11), 3563–3592, doi:10.1130/0016-7606(1973)84<3563:POSCIR>2.0.CO;2.

Nolet, G., and F. A. Dahlen (2000), Wave front healing and the evolution of seismic delay times, *J. Geophys. Res.*, *105*(B8), 19,043–19,054, doi:10.1029/2000JB900161.

Paulatto, M., T. A. Minshull, and T. J. Henstock (2010), Constraints on an intrusive system beneath the Soufriére Hills Volcano, Montserrat, from finite-difference modeling of a controlled source seismic experiment, *Geophys. Res. Lett.*, *37*, L00E01, doi:10.1029/2009GL041805.

Sanford, A. R., Ö. Alptekin, and T. R. Toppozada (1973), Use of reflection phases on microearthquake seismograms to map an unusual discontinuity beneath the Rio Grande rift, *Bull. Seismol. Soc. Am.*, *63*(6-1), 2021–2034.

Sato, H., I. S. Sacks, and T. Murase (1989), The use of laboratory velocity data for estimating temperature and partial melt fraction in the low-velocity zone: Comparison with heat flow and electrical conductivity studies, *J. Geophys. Res.*, *94*(B5), 5689–5704, doi:10.1029/JB094iB05p05689.

Sherrod, D. R., and N. S. MacLeod (1979), The last eruptions at Newberry Volcano, central Oregon, *Geol. Soc. Am. Abstr. Programs*, *11*(3), 127.

Sinton, J. M., and R. S. Detrick (1992), Mid-ocean ridge magma chambers, *J. Geophys. Res.*, *97*(B1), 197–216, doi:10.1029/91JB02508.

Stauber, D. A., S. M. Green, and H. M. Iyer (1988), Three-dimensional P velocity structure of the crust below Newberry Volcano, Oregon, *J. Geophys. Res.*, *93*(B9), 10,095–10,107, doi:10.1029/JB093iB09p10095.

Stroujkova, A., and P. Malin (2000), A magma mass beneath Casa Diablo? Further evidence from reflected shear waves, *Bull. Seismol. Soc. Am.*, *90*(2), 500–511, doi:10.1785/0119990071.

Toomey, D. R., G. M. Purdy, S. C. Solomon, and W. S. D. Wilcock (1990), The three-dimensional seismic velocity structure of the East Pacific Rise near latitude 9°30′N, *Nature*, *347*, 639–645, doi:10.1038/347639a0.

Toomey, D. R., S. C. Solomon, and G. Purdy (1994), Tomographic imaging of the shallow crustal structure of the East Pacific Rise at 9 30′N, *J. Geophys. Res.*, *99*, 24,135–24,157, doi:10.1029/94JB01942.

Turcotte, D. L., and G. Schubert (2002), *Geodynamics*, 2nd ed., Cambridge Univ. Press, New York.

Watanabe, T. (1993), Effects of water and melt on seismic velocities and their application to characterization of seismic reflectors, *Geophys. Res. Lett.*, *20*(24), 2933–2936, doi:10.1029/93GL03170.

Zucca, J. J., and J. R. Evans (1992), Active high-resolution compressional wave attenuation tomography at Newberry Volcano, central Cascade Range, *J. Geophys. Res.*, *97*(B7), 11,047–11,055, doi:10.1029/92JB00492.